Jurnal Tribologi 30 (2021) 24-43

MYTRIBOS Malaysian Tribology Society

Jurnal Tribologi

Website : jurnaltribologi.mytribos.org e-issn: 2289-7232

Effect of incorporation of nano-alumina on tribo-mechanical behavior of electroless Ni-B coatings

Deviprasanna Mohanty, Tapan Kumar Barman, Prasanta Sahoo *

Department of Mechanical Engineering, Jadavpur University, 700032 Kolkata, INDIA.
*Corresponding author: psjume@gmail.com

KEYWORDS

Corrosion
Electroless Ni-B
Friction
Nano- alumina
Nano-indentation
Wear

ABSTRACT

Electroless Ni-B coatings find versatile use due to high hardness and wear resistance that gets enhanced due to incorporation of hard nanoparticles. However, incorporation of nanoparticles suffers from high degree of agglomeration owing to small size and high surface energy. The present investigation aims at the deposition of electroless Ni-B-nano Al_2O_3 coatings using Sodium Dodecyl Sulphate (SDS) as surfactant and attempts to find the optimum amount of nano-alumina powder for superior tribo-mechanical characteristics. Thus, electroless Ni-B-nano Al_2O_3 coatings were prepared with varying concentrations of nano-Al_2O_3 (0 g/l, 2.5 g/l, 5 g/l, 7.5 g/l, 10 g/l, 12.5 g/l) in a chemical bath. To minimize agglomeration of alumina nanoparticles, ultrasonication technique was used. Coatings were characterized by Scanning electron microscopy (SEM), X-Ray diffraction (XRD) and Raman spectroscopy. Hardness, elastic modulus, wear resistance and corrosion resistance of the coatings were evaluated. Wear resistance and corrosion properties of the coatings show an improvement with the increase in the concentration of nanoparticles (Al_2O_3) in the bath up to 10 g/l but on further increasing the concentration to 12.5 g/l deterioration in wear resistance and corrosion resistance is observed. As compared to binary Ni-B coating, the coating prepared with 10 g/l concentration of nanoparticles shows an increase of around 30% and 60% for Vicker's microhardness and elastic modulus, respectively. The optimum amount of alumina nano-powder in the coating bath is thus found as 10 g/l considering superior elastic modulus, corrosion resistance and wear resistance.

Received 21 May 2021; received in revised form 25 June 2021; accepted 2 August 2021.
To cite this article: Mohanty et al. (2021). Effect of incorporation of nano-alumina on tribo-mechanical behavior of electroless Ni-B coatings. Jurnal Tribologi 30, pp.24-43.

1.0 INTRODUCTION

Wear and corrosion are the primary reasons for material damage in industries. Surface modification by coatings is a viable option to protect such materials that are exposed to tribological contacts and environmental degradation. Electroless coating is one such alternative that protects the material from decay due to wear and corrosion. Also, the incorporation of a hard particle into the electroless Nickel-Boron (ENB) coating further improves hardness, abrasion resistance, wear resistance and corrosion resistance of the resulting coatings (Barati & Hadavi et al, 2020 ; Sudagar et al, 2013; Narayanan and Seshadri, 2004; Georgiza et al, 2017; Krishnaveni et al, 2012; Mukhopadhyay et al, 2016; Mukhopadhyay et al, 2018). ENB coatings deposit under a controlled pH and temperature in presence of Ni-source ions, reducer, complexing agent, stabilizer and activator. The uses of electroless plating process include VLSI (Very large scale integrated) technology, decorative plating, electromagnetic shielding, automotive, functional coatings for chemical oil and gas, and aerospace industries, food, petrochemical, computer and printing, and plastics industries (Mukhopadhyay et al, 2018; Barman et al, 2019; Shakoor et al, 2016; Celik et al, 2016; Dominguez-Rios et al, 2012; Bulbul et al, 2012; Das and Sahoo, 2011; Sahoo and Das, 2011). Several researchers have studied the effect of heat treatment on the hardness and tribo-behavior of ENB coatings and have concluded that both hardness and wear resistance improved on heat treatment (Vitry & Bonin, 2017; Pal & Jayaram, 2018). But others have also pointed out the adverse effect of temperature on the corrosion resistance of these coatings. Dervos et al. (2004) observed that cracking occurred in the Ni-B coatings at high temperatures (850^{o}C) causing an increase in corrosion rate. Abdel-Gawad et al. (2019) have also reported the decrease in corrosion resistance of the Ni-B-Sn coating due to the loss of amorphosity at 400^{o}C. Hence research attempts have been made to deposit coatings with improved wear resistance as well as corrosion resistance. One way to ensure improved corrosion resistance is with the addition of nanoparticles. Improved corrosion resistance was observed due to the incorporation of CeO_2 (Pancrecious et al, 2018) and SiC (Georgiza et al, 2017) into Ni-B coatings. The challenge involved in the deposition of nanoparticle reinforced coatings is the uniform distribution of the nanoparticles in the coatings. As reported for electroless Ni-P-Alumina coating, an inhomogeneous distribution results in defects such as voids, internal stresses, and discontinuities (Leon-Patino et al, 2019). To address this issue, a combined effect of ultrasonic agitation and surfactant may be attempted. The ultrasonic agitation ensures deagglomeration of nanoparticles thus they are well dispersed in the solution bath which results in a homogenous coating and the surfactant ascertains that the nanoparticles remain suspended in the bath throughout the coating duration, avoiding sedimentation (Mahbubul et al,2019; Ordóñez et al, 2020).

Alumina is one of the most prolific reinforcement material used in the case of surface modification of coatings as well as composite materials (Purohit and Vagge, 2016; Sarbishei et al, 2016; Mahdavi et al, 2020). Owing to the high hardness of alumina particles, the incorporation of these particles results in improved mechanical properties like hardness and elastic modulus in composite materials. Besides this, these particles also increase the wear resistance. The literature although provides ample observation on electroless Ni-P-Alumina coatings, a lacuna persists in regard to the Ni-B-nano Alumina coatings. Li et al. (2018) have investigated the effect of alumina reinforcement on the hardness and corrosion resistance of electrodeposited Ni-B coatings. Ekmekci and Bulbul (2015) have studied the nano alumina reinforced electroless Ni-B, but their investigation is limited to the characterization of these coatings. The literature lacks a detailed investigation into the wear behavior and mechanical properties of Ni-B-nano Alumina coatings. Furthermore, a study into the correlation of these mechanical properties to the colloidal stability

of the alumina nanoparticles in the solution has not been explored yet. Besides, the present research also attempts to find the effect of varying concentrations of nano alumina on the mechanical behavior of electroless Ni-B coatings. To the best of authors' knowledge, no work has been reported on these aspects.

The present study aims at incorporating varying amounts of nano alumina particles into the Ni-B coatings. The resulting coatings were subjected to various characterization techniques such as X-Ray diffraction pattern analysis, Raman spectroscopy and analysis of scanning electron micrographs combined with the EDX study. Additionally, the coatings undergo hardness testing, elastic modulus evaluation via nano-indentation method, wear study (behavior and mechanism) and electrochemical corrosion testing. It is expected that the reinforced coatings would perform better as compared to the unreinforced counterpart. Besides, the study also aims at finding an optimum alumina concentration in the bath to obtain a coating with good mechanical properties along with improved wear and corrosion resistance.

2.0 EXPERIMENTAL PROCEDURE

The as-received alumina nano-powders (20-30 nm) were first sonicated in presence of Sodium Dodecyl Sulphate (SDS) in deionised water to form a colloidal suspension of alumina particles. SDS is a suitable surfactant for the dispersion of alumina particles (Xu et al, 2017). The ultrasonication was done using a probe-type sonicator at a frequency of 60 kHz and 120 W. Sonication was carried out for one hour until a proper colloidal state was reached and the particles do not settle to the bottom. Before the coating process, the alumina colloidal solution was subjected to a zeta potential test using a Zetasizer Nano ZS (Malvern, United Kingdom) to determine the saturation concentration of alumina in the coating bath. Ni-B-Nano alumina with varying alumina concentration namely: 2.5 gm/l, 5 gm/l, 7.5 gm/l, 10 gm/l and 12.5 gm/l were deposited using a basic bath solution. The constituent bath elements are presented in Table 1. The coatings were deposited at a temperature of 85 °C ± 3 while keeping the bath continuously agitated at 300 rpm. All the coatings (Table 2) were deposited for duration of 1 hr.

Table 1: Coating bath composition.

Sl. No.	Chemical	Manufacturer	Function	Amount in bath
1.	Nickel chloride	Merck (US)	Nickel source	18-20gm/l
2.	Ethylene diamine	Merck (US)	Complexing agent	45-50 ml/l
3.	Lead nitrate	Merck (US)	Stabilizer	0.05-0.06 gm/l
4.	Sodium hydroxide	Merck (US)	Maintains pH	35-40 gm/l
5.	Sodium borohydride	Merck (US)	Reducing agent	0.5 gm/l
6.	Nano alumina	SRL Chem (India)	Reinforcement	Varying amount
7.	SDS	SRL Chem (India)	Surfactant	2.36 gm

* The bath temperature was maintained at 85°C ± 3.

Table 2: Coating nomenclature.

Sl. No.	Description of the coating	Nomenclature
1.	Ni-B binary coating	Ni-B
2.	Ni-B + 2.5 g/l nano alumina	Ni-B-2.5
3.	Ni-B + 5 g/l nano alumina	Ni-B-5
4.	Ni-B + 7.5 g/l nano alumina	Ni-B-7.5
5.	Ni-B + 10 g/l nano alumina	Ni-B-10
6.	Ni-B + 12.5 g/l nano alumina	Ni-B-12.5

Post coating, the coated specimens were subjected to Raman spectroscopy using a Raman spectrometer (Renishaw Invia, UK) which employs an Argon laser that has an excitation wavelength of 514 nm. These parameters are appropriate for recording the Raman spectra of thin films and embedded nanoparticles (Mandal et al, 2016). The retention of alumina in the coatings was established by identifying the characteristic alumina peaks in the obtained spectrum. The amorphous nickel phase was identified by XRD (Bruker D8 advance, USA). The operating parameters are as follows: current 40 mA and voltage 45kV. The target to obtain the X-Ray diffraction pattern was Cu-Kα (λ_{Cu} = 1.54A°). The diffraction angle ranged from 35° to 60°. The visual imaging was done using a scanning electron microscope (Zeiss Evo 18, Germany). The instrument has a tungsten filament and is capable of resolving up to 50 nm hence a magnification of 50K to 100K may be reached (depending on the specimen).

Determination of the corrosion resistance of the coatings was carried out by subjecting the coatings to an electrochemical corrosion test. The corrosive environment used was a standard 3.5 wt % sodium chloride solution in deionised water. The Tafel curves were generated using a potentiostat (ACM Instruments GILL AC, UK) and analyzed by the Origin software (version 2016). The tests were conducted using the three-electrode potentiodynamic polarization technique, which is a known standard for such coatings (Mohanty et al, 2019; Manning, 1980). A saturated calomel electrode (Secondary electrode), working electrode (coated specimen) and a platinum electrode (counter electrode) are employed to perform the test. The specimens were scanned at a rate of 1mV/s during the potentiodynamic test.

The microhardness tester employs a pyramid type diamond indenter. Microhardness measurements were done using a Vicker's microhardness tester (UHL VMHT, Germany). The applied load, dwell time and indenter travel speeds are 100 gmf, 15s and 25 μm/s, respectively. An average microhardness for 10 readings is reported here. The elastic modulus was evaluated using a Nano indenter (CSM NHT-1, USA). This is a tabletop model which employs a triangular-based diamond Berkovich indenter to make the indentations. The maximum depth of indentation was fixed at 100 nm and the loading and unloading rate was fixed at 20 mN/min. The test was repeated thrice, and an average value of the elastic modulus obtained is presented in this research.

Tribo test was conducted on a Ducom wear and friction monitor (Ducom TR-208-M2, India). The tribotester used is a pin-on-disc type model in which a hardened EN31 disc acts as the rubbing counterface and the cylindrical coated specimens acted as the pin. The speed and sliding distance were kept fixed at 100 rpm and 500 m, respectively. Results were obtained for two load variations, 1 kgf and 2 kgf. Each test was repeated thrice and the average weight loss due to wearing is reported in this study. Any wear debris stuck to the counter disc was cleaned off with acetone. This ensured an error-free data acquisition during the test. The pin-on-disk test was performed adhering to the standard of ASTM G99. Prior to the wear test the uncoated test coupons were

polished by different grades (400, 800, 1600 and 2000) of emery paper. Polishing helped to maintain parity in the surface roughness of the samples before coating. This in turn, eliminated any alterations that roughness might cause to the friction and wear data. The reinforced coatings were finally compared to the binary Ni-B coating to demonstrate the need for reinforcements.

3.0 RESULTS AND DISCUSSION

3.1 Effect of Surfactant on The Stability of Alumina Colloidal Solution

Alumina nanoparticles of 20-30 nm average diameters were commercially obtained. Figure 1 (a) shows the alumina suspension in the absence and presence of surfactant (SDS). The addition of SDS helps to keep the nanoparticles suspended in the solution for days, while the solution without surfactant can be observed with sedimentation at the bottom of the beaker. This ability to keep the particle suspended allows the nanoparticles to be embedded in the coating during the deposition. Figure 1(b) shows the SEM of dry un-sonicated agglomerates of alumina powder. Zeta potential is the surface potential of the nanoparticles relative to the boundary of the diffused layer when the particle is in suspension. Any nanoparticle in suspension with a surface charge tends to form a double layer by attracting oppositely charged ions towards its surface.

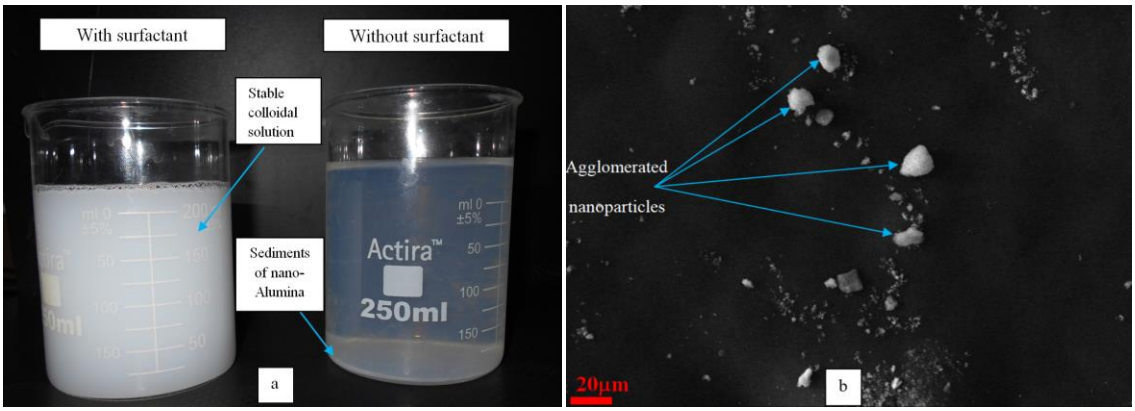

Figure 1: (a) Image of a colloidal suspension of alumina particles after allowing it to settle for 4 hours, in presence and absence of sodium dodecyl sulphate (SDS); (b) SEM image of nano Al_2O_3 agglomerates.

Figure 2 shows the schematic diagram of a typical nanoparticle with a negative surface charge. It attracts positive ions which get attached, in a dense packing, adjacent to the surface. This layer is known as the stern layer. The stern layer is followed by the diffused layer, with loosely held ions. The potential difference between the boundary (slipping plane) of the outer diffused layer and the particle surface gives an electrokinetic potential difference between the two layers known as the zeta potential (ISO 13099-12012(E), 2012). Zeta potential is a standard for defining the stability of particles in colloidal suspensions (Lu and Gao, 2010; Jiang et al, 2009). In general, a zeta potential value of ±40 to ± 60 of a suspension is considered as having good stability. A value of ±30 to ± 40 is considered to represent a colloidal suspension of moderate stability (Hunter, 2013; Kumar and Dixit, 2017; Freitas et al, 1998). A zeta potential value in the range of ±10 to ±30 is considered as representing a suspension with insipient stability and any value below this range,

i.e., 0 to ±10 causes flocculation in the suspension and results in the sedimentation of the submerged particles.

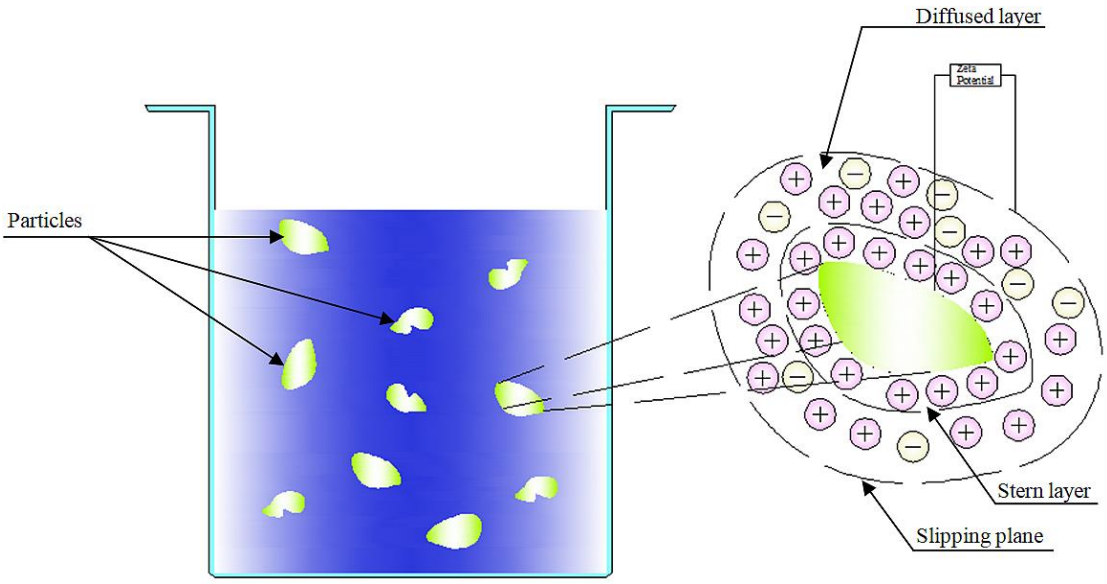

Figure 2: Schematic drawing showing a typical suspended particle surrounded by ions forming the basis for zeta potential measurement.

A surfactant comes in handy in situations where the suspended particles need to remain suspended for a long duration, which is a requirement of electroless coating. The presence of surfactant also improves the wettability of the particles (Maestro et al, 2015). The surfactants are adsorbed onto the solid particulate surface and provide an overall charge to the engulfed particles. As a result, all particles of similar nature tend to possess like charges of finite magnitude on their periphery. This causes repulsion of like particles and prevents flocculation. Thus, the suspended particles do not coagulate and remain suspended for a longer duration of time. Figure 3 shows a schematic diagram of a lone alumina particle surrounded by surfactants that impart a net charge on to the surface. Figure 4 shows the measure of zeta potential of nano alumina of varying concentrations at a pH of 12, which is the solution bath pH of the coatings under study. The zeta potential was measured in the presence and absence of surfactants. The surfactant used is Sodium Dodecyl Sulphate (SDS), anionic surfactant. It was observed that the zeta potential value changed from a moderate stability solution potential to a good stability solution potential. This is attributed to the ability of the surfactant to wet solid surfaces as well as its ability to impart a net charge (in the present case, a negative charge) to the particles. The zeta potential value drops beyond alumina concentration of 10 g/l. With the increase in concentration of alumina to 15 g/l the zeta potential value significantly decreased from a good colloidal stability zone (-52 mV) to a moderately stable zone (-39 mV), for the solution with surfactant. This could be due to the agglomeration of nanoparticles. These nanoparticles owing to their high surface charge tend to agglomerate if there is a high concentration of such particles in the solution. In the present case, beyond 10 g/l of alumina nanoparticles are unable to stay suspended in the solution, at a pH of 12. Due to the decrease in stability of these solutions beyond the alumina concentration of 10 g/l,

the properties such as elastic modulus, wear resistance and corrosion resistance of the coatings (prepared from 12.5 g/l of alumina concentration) deteriorated.

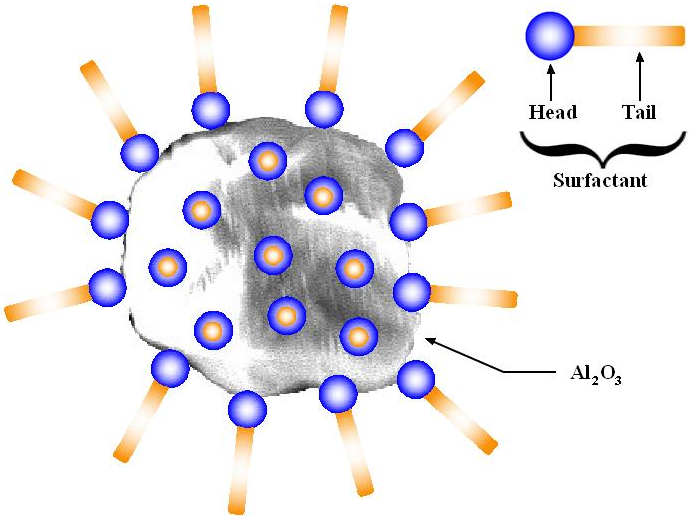

Figure 3: Schematic diagram of lone alumina particle surrounded by surfactant.

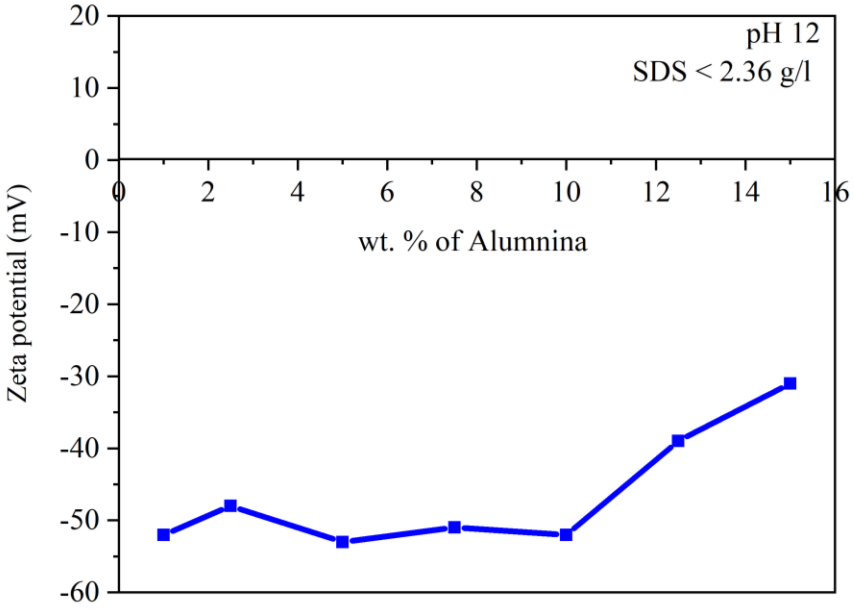

Figure 4: Variation of zeta potential with alumina wt % in a solution of pH 12.

3.2 Coating Morphology

Figure 5 shows the coating morphology identical to cauliflower-like nodules spread throughout the surface. Various literature reported that addition of nanoparticles has a bearing on the nodule size in addition to improvement in the hardness and wear resistance of the EN coatings (Islam et al, 2015; Yu et al, 2011). Figure 5(a) to Figure 5(f) show typical nodular microstructure which is a characteristic feature of electroless coatings. Figure 5(a) for Ni-B binary coating shows larger nodules as compared to reinforced coatings shown in Figure 5(b) to Figure 5(f). The decrease in size of the nodular structure may be due to the structural refinement brought about by the inclusion of alumina nanoparticles. Although no clear trend in the nodular size could be established among the reinforced coatings, it can be concluded that as compared to the binary Ni-B coating the reinforced coatings show a more refined nodule. Figure 6 (a) shows agglomerated alumina nanoparticles perched on the coating surface partially or completely covering the nodular gaps. Several patches of agglomerated alumina nanoparticles (denoted by X in Figure 6(a)) can be seen blanketing the nodular gaps partially or fully. This forms an impermeable layer of Ni-B matrix and nano-alumina reinforcement protecting the substrate. Ernst et al. (1997) reported that electroless coatings are dense as the coating grows by overlap of nodules. As can be observed from Figure 6 (a) the nanoparticles seem to have embedded themselves in the nodular gaps and micro porosities of the Nickel–Boron matrix. Figure 6 (b) depicts the EDX map of the Ni-B-10 coating subsurface. Prominent Aluminium K-α peaks can be observed in the EDX pattern. The presence of sodium is due to the addition of sodium hydroxide which is used to keep the pH value of the bath solution basic.

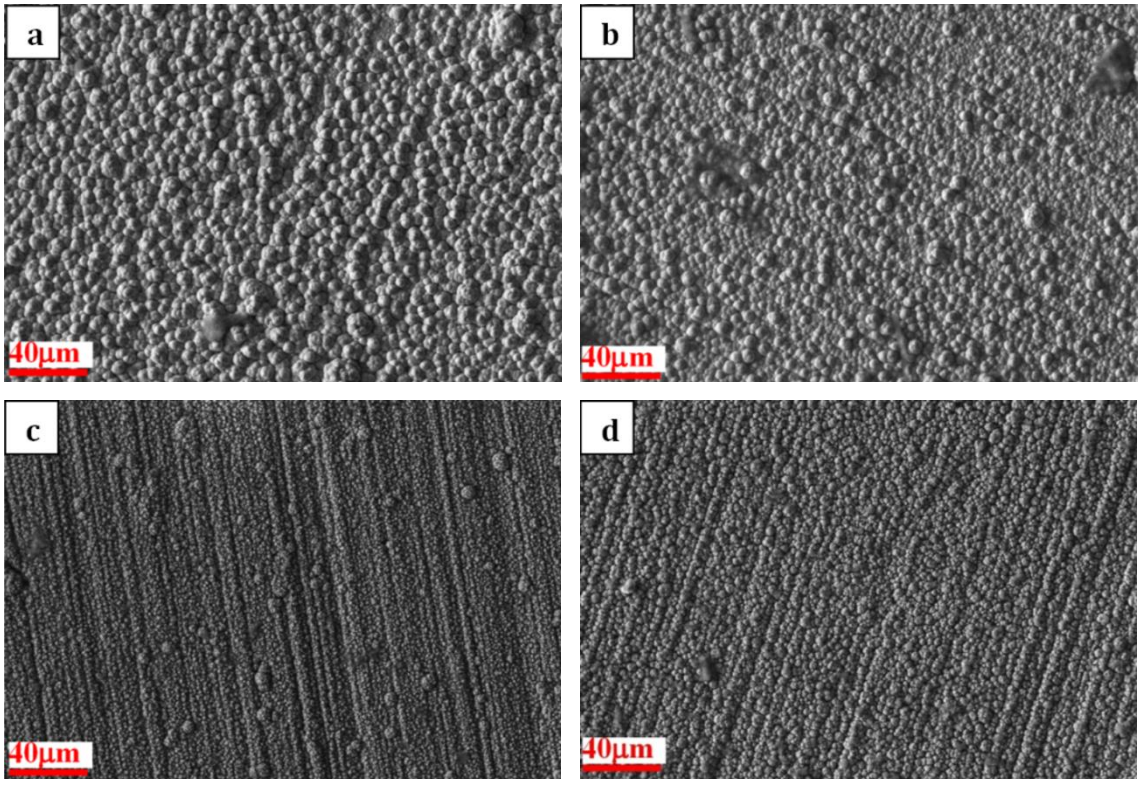

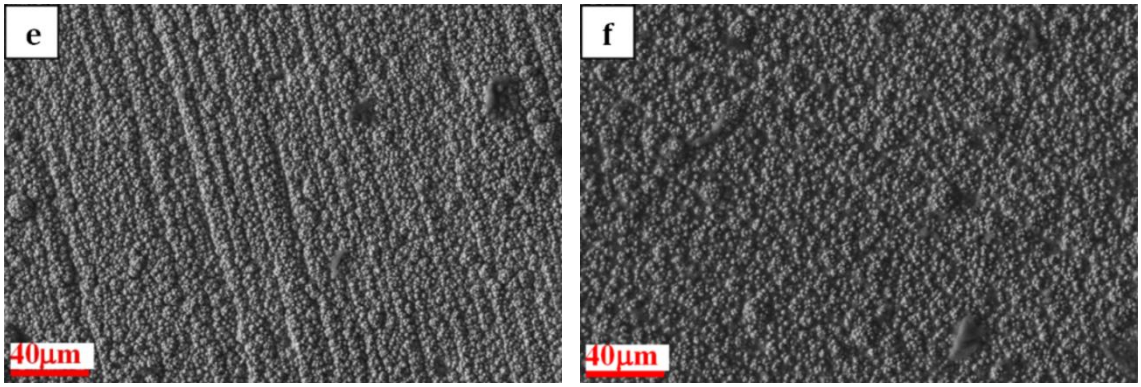

Figure 5: SEM images (2000X) of nodular microstructure of (a) Ni-B, (b) Ni-B-2.5, (c) Ni-B-5, (d) Ni-B-7.5, (e) Ni-B-10 and (f) Ni-B-12.5 .

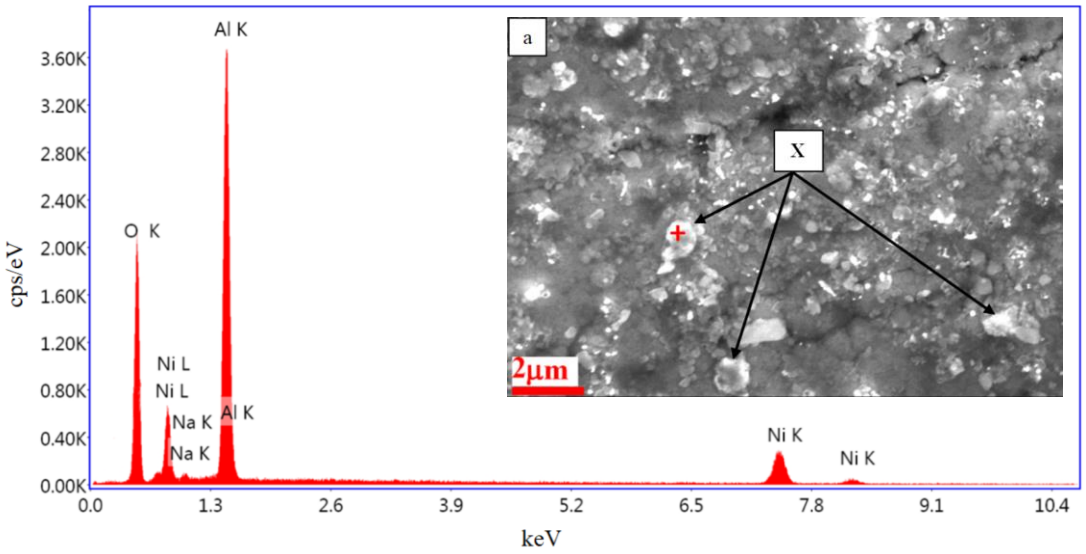

(b)

Figure 6: (a) SEM image (10000X) of the subsurface region of the Ni-B-10 coating, (b) point EDX of the coating surface (marked by '+').

3.3 Raman Spectroscopy

Figure 7 depicts the Raman spectroscopy of the coated samples. The peaks signify the presence of a stable α-Al_2O_3 and not the γ- Al_2O_3. According to Laha et al. (2005), the γ- Al_2O_3 does not show any visible peak in the Raman spectrum. The band at 539 cm-1 shows the characteristic peaks of α-Al_2O_3, while the bands at 321 cm^{-1} and 306 cm^{-1} show the spectrum corresponding to $Al(OH)_3$ (Ruan et al, 2001). This is quite possible as the electroless deposition is performed in a solution with deionised water as the solvent. The coating bath temperature is maintained at around 85°C,

which facilitates the chemical bonding of alumina with water and results in the formation of the hydroxide. The band at 539 $cm^{-1}$and 446 cm^{-1} correspond to Al-O-Al distortion and the ones at 321 cm^{-1} and 306 cm^{-1} are used by stretched vibrations due to the formation of Al-O bonding. Raman data is significant to the study because due to the low percentage of adsorption of alumina into the coating it often becomes difficult to identify the alumina peaks by the X-Ray diffraction method.

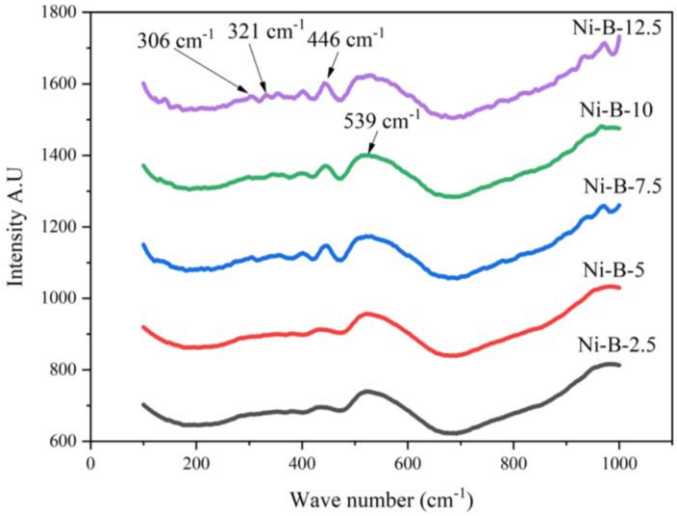

Figure7: Raman spectrum of the coated specimens.

3.4 X-Ray Diffraction

The diffraction pattern analysis of the coatings under study is shown in Figure 8. XRD helps identify the nature of as-deposited coatings. In the present case, a broad peak with low intensity (peak height) at around 45° (JCPDS No. 01-070-1849) was observed. This indicates that the Ni atoms lack periodicity (suggesting typical amorphous nature) in their arrangement inside the coating. In the case of amorphous solids when the sample is rotated through a range of scanning angles, the diffracted rays do not pile up to form a constructive interference, as a result of which the intensity of the peak is low (Cullity & Stock, 2001). Also, according to Cullity & Stock (2001), XRD of amorphous or semicrystalline solids results in the formation of broader peaks as compared to crystalline solids. Such broad Ni peaks with low intensity have also been reported elsewhere (Mukhopadhyay et al, 2019; Yildiz et al, 2021).

Although as reported by Delaunois and Lienard (2002), the structure is often found to be a mixture of crystalline and amorphous structures. Dervos et al. (2004) and Ziyuan et al. (2006) also supported the presence of the mixed structure in electroless coatings. The identification of boron tends to be difficult via XRD because of the low solubility of boron in solid nickel (0.03 wt %) (Hamid et al, 2010). The boron is often identified in the form of some Ni-B inter-metallic as Ni_3B and Ni_2B when the coatings are subjected to heat treatment. It can be deduced from the XRD pattern that the addition of alumina does not affect the structure of the coating although it may change the morphology of the coatings (from coarser to finer nodules) (Hu et al, 2018).

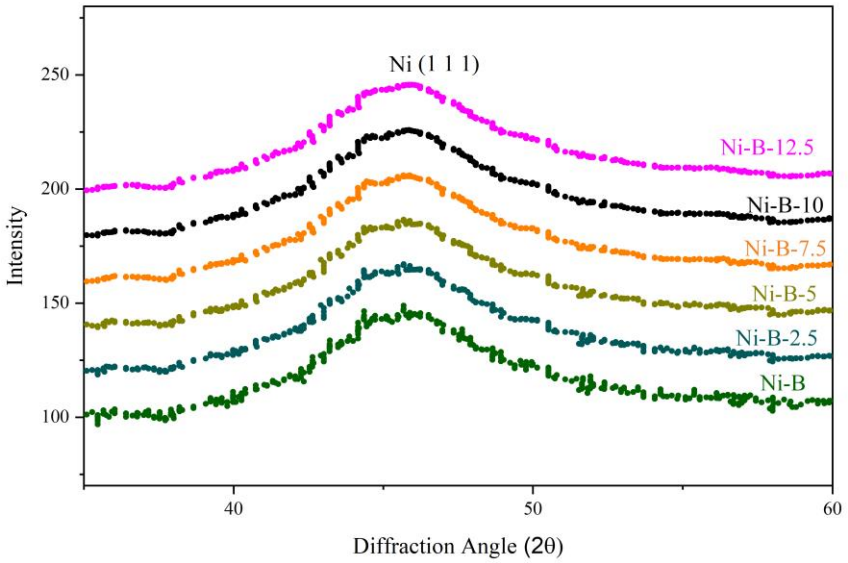

Figure 8: X-Ray diffraction of the specimens under study.

3.5 Micro Vicker's Hardness and Nano-Indentation

Figure 9 (a) shows the hardness values obtained for the coatings. With the addition of nano Al_2O_3, the hardness increases as expected. This is attributed to the desired hard nanoparticle inclusion, which when embedded in the softer Ni-B matrix, transfers the applied load from the matrix to the reinforcements (nano Al_2O_3). This sharing of load causes a hardness value. Further, these nanoparticles obstruct the flow of material when a load is being applied during hardness test this also helps to restrict the size of indentation as a result a higher value of hardness is obtained. Although the hardness improves with the addition of nanoparticles it should be noted that the standard deviation of the hardness values for the coating Ni-B-12.5 is much higher than the other coatings as indicated by the error bars. This fluctuation in hardness values is a result of the inhomogeneous distribution of nano-Al_2O_3 powders in the case of the Ni-B-12.5 coating caused by the higher degree of agglomeration of alumina beyond a concentration of 10 g/l. Figure 9(b) represents the elastic modulus in graphical format. The elastic modulus increases with the addition of nano-particles. Unlike the hardness a clear trend is not observed for the elastic modulus values. The elastic modulus (E) increases from 75.9 GPa for binary Ni-B to 122.9 GPa for the reinforced Ni-B-10 coating. This may be due to the dispersion strengthening resulting from the addition of nanoparticles (Mahdavi et al, 2020; Li et al, 2018).

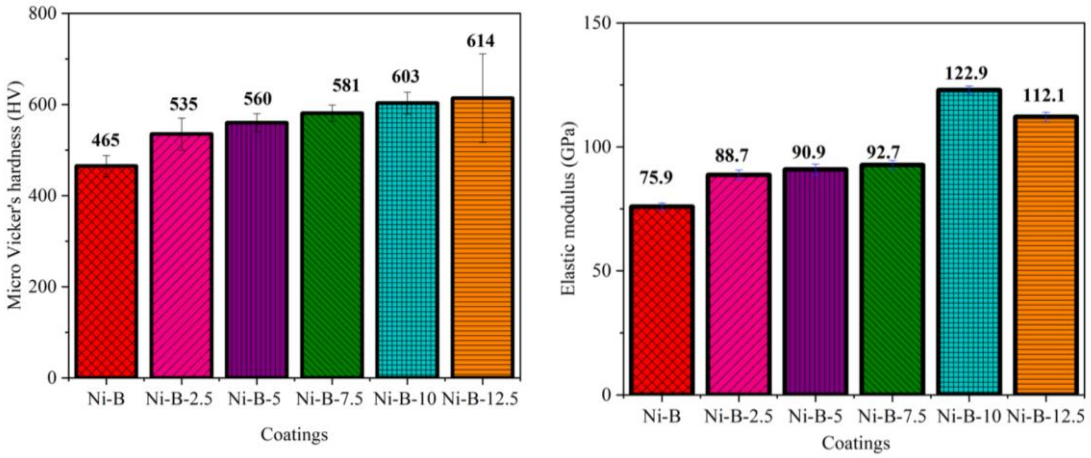

(a) (b)

Figure 9: (a) Micro Vicker's hardness of coatings taken at 100 gf load, (b) elastic modulus of the coatings obtained at a loading-unloading rate of 20mN/min.

Figure 10 shows the loading/unloading curve for the variation of normal force against the applied depth of penetration of the indenter. The curve is obtained by employing the depth method. In this method, the load is allowed to vary up to a maximum depth of 500 nm and once the maximum depth is reached the load is released. The loading and unloading rates were maintained at 20mN/min. The pattern of the curves obtained is quite similar to one another. The area under each curve represents the energy absorbed by the respective coating to reach the desired penetration depth of 500 nm. The loading-unloading curve for Ni-B-10 coating encompasses the largest area among the coatings. This is also corroborated by its elastic modulus value of 122.9 GPa which is the largest for the coatings under study. It must be noted that although the percentage addition of alumina in the coating bath of Ni-B-12.5 is more (12.5 g/l) as compared to Ni-B-10 coating, still the resulting elastic modulus is less as compared to Ni-B-10. In the present case, due to the excessive agglomeration of alumina (beyond 10g/l concentration), proper inclusion and uniform distribution of alumina may not be achieved in the Ni-B-12.5 coatings, as a result, lower dispersion strength and a lower elastic modulus are obtained. It should be mentioned here that more alumina in the coating bath does not necessarily mean more absorption of alumina in the coating. The absorption of alumina depends on the degree of agglomeration and sedimentation of the colloidal solution. Due to the higher degree of agglomeration in case of the bath containing 12.5 g/l of alumina, the Ni-B-12.5 showed some erratic results during hardness test. This may be attributed to the inhomogeneous distribution of alumina on the coating surface. As a result, when the indenter indented on these agglomerated patches of alumina high hardness value was obtained but when the indentation was on the softer matrix where there was no alumina present low hardness value was obtained. This may have caused the fluctuation in hardness values for Ni-B-12.5 as compared to other coatings in the study.

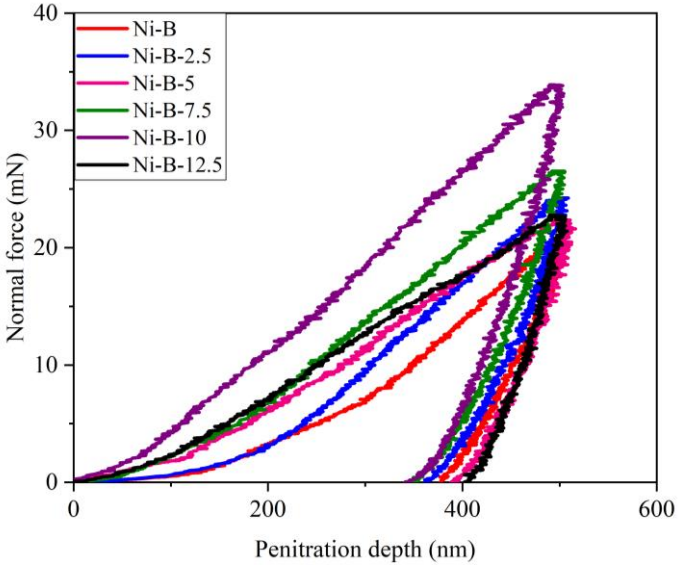

Figure 10: Loading and unloading curve showing the variation of normal force with the penetration depth.

3.6 Tribological Behavior

The coatings under study were subjected to a dry sliding wear test at loads of 1 Kgf and 2 Kgf and a sliding speed of 100 rpm. The specific wear rates at these loads are shown in Figure 11(a) and 11(b). These figures show that with the increase in the amount of reinforcement (nano alumina) from 0 g/l to 10 g/l in the coating bath, the wear resistance of the coatings also increases. This is due to the increase in the percentage inclusion of hard nanoparticles in the coating. The hard alumina nanoparticles when embedded in the softer Ni-B matrix obstruct the sliding motion and do not allow the interacting coating surface to be removed easily. The corresponding data for the variation in frictional force is shown in Figure 12. Here the increase in frictional force along with the addition of nanoparticles is evident. However, there seems to be a break in trend at 12.5 g/l of alumina in addition to the coating. At points, 'a' and 'b' in the Figure 12 a sudden drop in frictional force is visible for coating reinforced with 12.5 g/l alumina. This may be due to the pluck out of patches of nanoparticles from the coating surface. This makes the coatings weak and subsequent removal of the coating layer occurs at certain instances. The alumina patches are formed as a result of excessive agglomeration. As discussed earlier, beyond 10 g/l wt the agglomeration of alumina becomes severe which is detrimental to the stability of the colloidal solution and the suspension stability of nano alumina in the coating bath. Also, there are instantaneous spikes in frictional force at certain points as seen in Figure 12. This is more evident in the case of the coatings with a higher concentration of nanoparticles (10 g/l and 12.5 g/l). This may be attributed to the three-body abrasion caused due to the reattachment of the plucked-out nanoparticles back into the softer matrix of the specimen surface. Figure 13 shows the worn surface of the coatings. A similar mechanism can be observed in all the coatings. A combination of abrasive and adhesive wear seems to be the dominating wear phenomenon (Gawne and Ma, 1987; Correa et al, 2013). Figure 13 also shows micro-cracks and pluck out of worn patches due to the sliding motion and interaction of the coatings with the hard EN 31 counterparts.

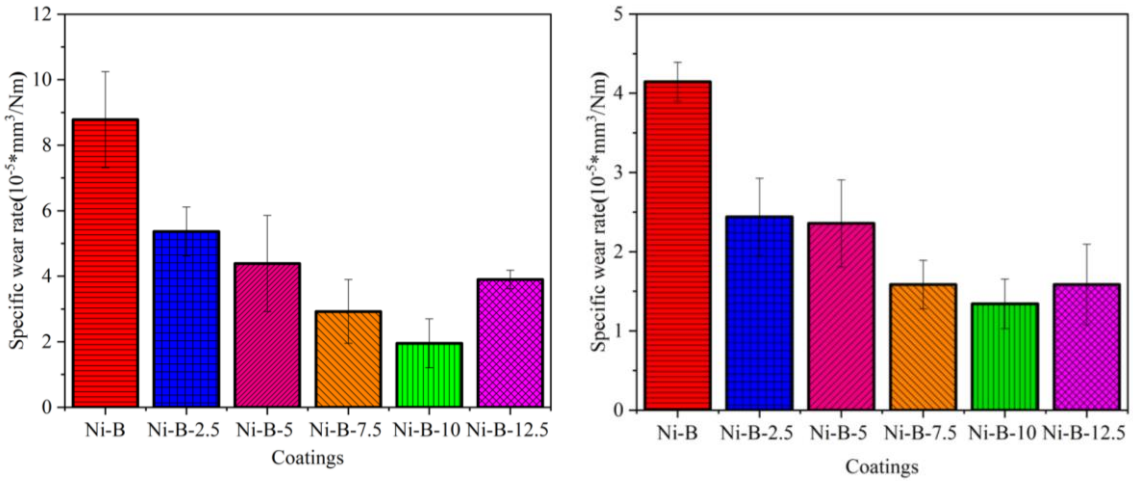

Figure 11: Specific wear rate of the specimen under a load of (a) 1 kgf and (b) 2 kgf.

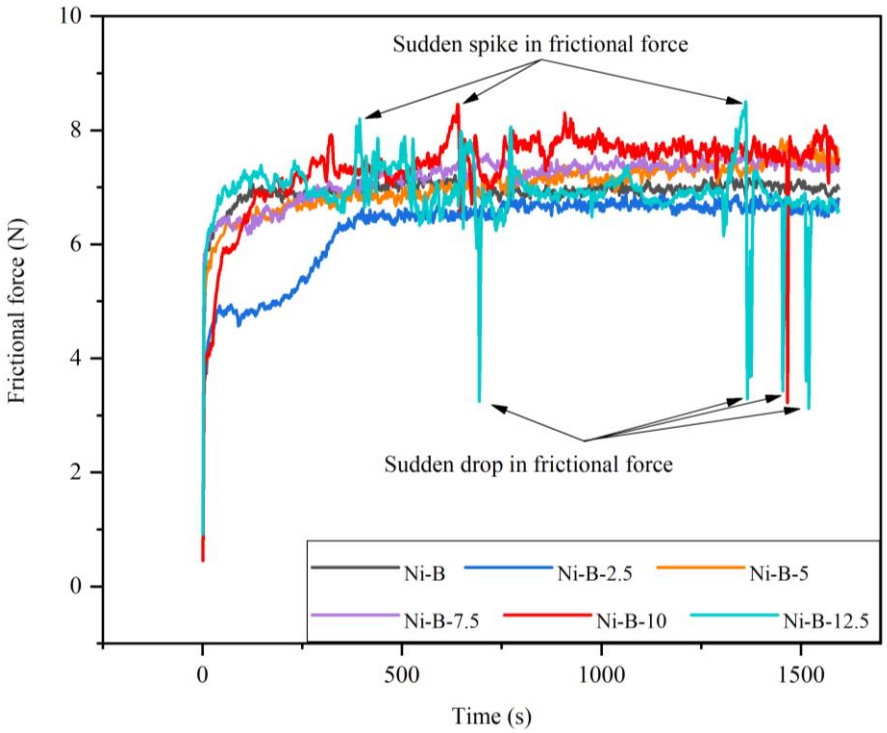

Figure 12: Variation of frictional force with time for the coatings under study.

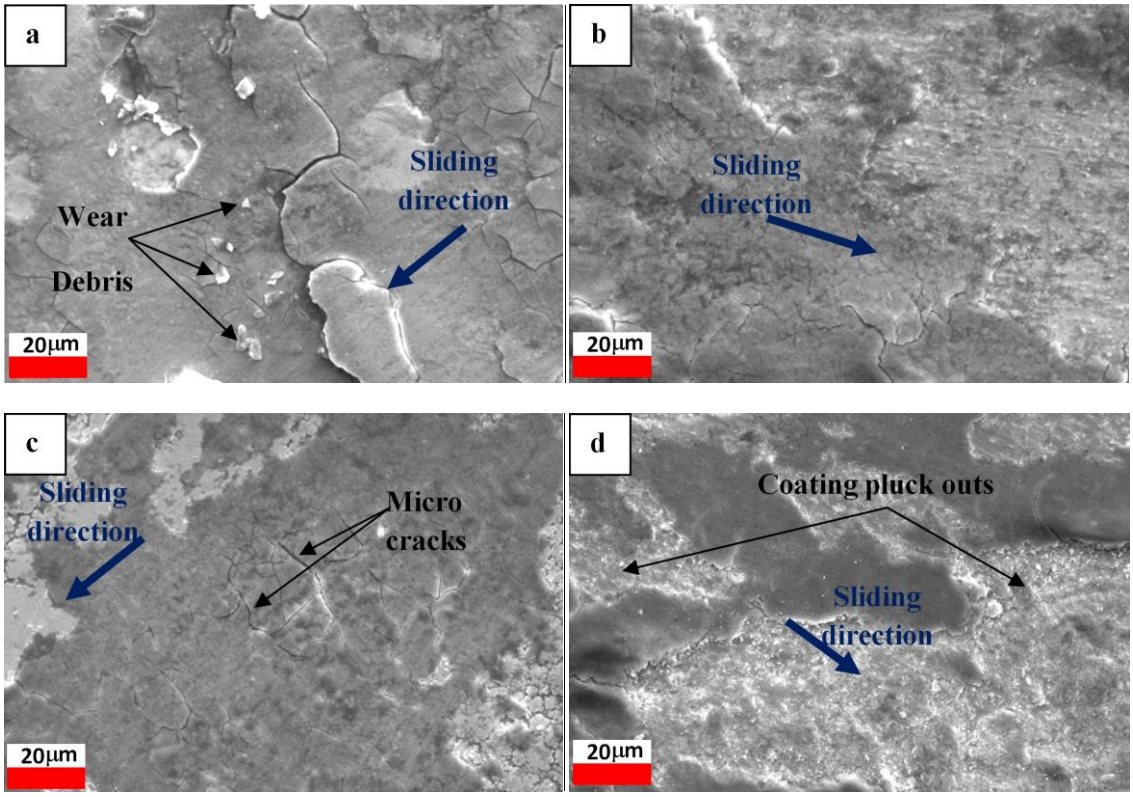

Figure 13: Wear morphology of (a) Ni-B, (b) Ni-B-5, (c) Ni-B-10 and (d) Ni-B-12.5.

3.7 Corrosion

Electroless coatings are highly corrosion resistant. These coatings do not act as sacrificial layers instead they form a noble and almost impervious layer upon the substrate. Thus obstruct the substrate from coming directly in contact with the corrosive environment. To achieve this, the coatings need to be non-porous. An added advantage of these coatings is the absence of any grain boundaries that act as inherent sites for excessive corrosion (Sha et al, 2011). Hamid et al. (2010) discussed the detrimental effect that heat treatment has on the electrochemical corrosion resistance of the EN coatings. They found that although heat treated coatings show improved surface micro-hardness and increased sliding wear resistance but due to warping of the coatings, heat treatment tends to decrease the corrosion resistance. The improved micro-hardness and wear resistance is attributed to the formation of hard inter-metallic phases like Ni_3B and Ni_2B and also the transformation of coatings to a more or less crystalline structure from an amorphous structure of the as-deposited coatings. A high temperature of 800 °C and above tends to cause severe flaking due to the decrease in adhesion of these coatings with the underlying substrate layer (Biswas et al, 2017). Hence, for optimal design, parity has to be maintained between the mechanical properties and corrosion behavior of these coatings.

Figure 14 shows the Tafel curves for the coatings under study. The corrosion current increases along with the incorporation of alumina nanoparticles until the Ni-B-10 but start to decline as the amount of alumina is further increased in the bath. This may be attributed to the agglomeration of nanoparticles which reduces the effective surface covered by the nanoparticles as compared to

the case when they are more or less dispersed (as is for the coatings with a lower amount of alumina addition). The best performing coating in this study per corrosion protection is Ni-B-10 because, with the further addition of alumina (12.5 g/l) to the coating bath, the colloidal solution tends to display insipient stability as shown by the zeta potential value in Figure 4. The E_{corr} value increases from -494.54 mV (binary Ni-B coating) to a nobler (more positive value) value of -421.02mV for the Ni-B-10 coating. This shift of corrosion potential is also an indicator of the improved corrosion resistance of the Ni-B-10 coating. Although researchers argue that I_{corr} value provides a better representation of the electrochemical corrosion behavior of surfaces, in the present research in addition to the corrosion current the corrosion potential also follows a similar trend. This is strong evidence in favor of the improved corrosion potential of the reinforced specimens. As observed from Table 3, E_{corr} value suggests a decreased performance of Ni-B-12.5 coating against 3.5% NaCl solution used as the corrosive environment.

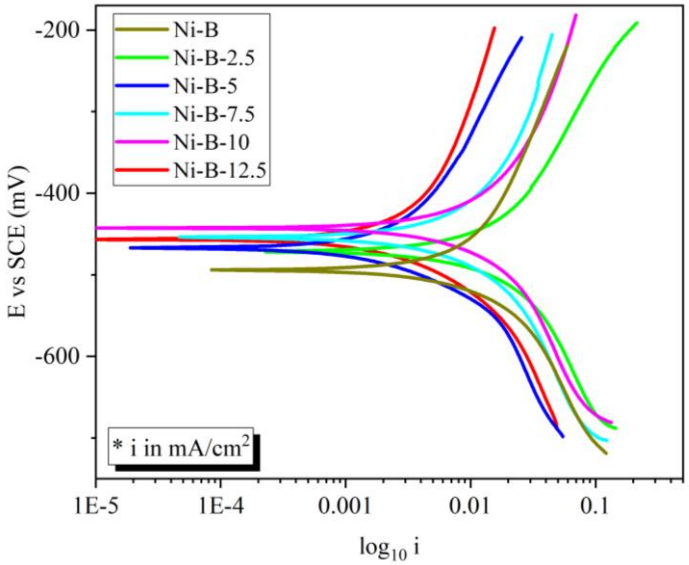

Figure 14: Tafel curves (Anodic and cathodic) for the coatings under investigation.

Table 3: Corrosion potential and current for the coatings under study.

Sl. No.	Specimen	E_{corr} (mV)	I_{corr} (mA/cm^2)
1	Ni-B	- 494.54	0.01126
2	Ni-B-2.5	- 471	0.01103
3	Ni-B-5	- 467.64	0.009
4	Ni-B-7.5	- 458.08	0.004
5	Ni-B-10	- 421.02	0.0026
6	Ni-B-12.5	- 456.83	0.0092

4.0 CONCLUSIONS

The present study evaluated the influence of the addition of alumina nanoparticles on the microhardness, elastic modulus, wear resistance and the electrochemical response of the coatings. The improvement in the properties was brought about by the dual effect of improved hardness and refinement of the nodular morphology of the coatings. Following are the conclusions drawn from the study:

(a) The addition of alumina nanoparticles increased the microhardness of the coatings. The maximum microhardness of 614 HV was observed for the coating Ni-B-12.5.
(b) As compared to Ni-B coating, the elastic modulus is observed to increase by approximately 62% and 48% for Ni-B-10 and Ni-B-12.5 coatings, respectively.
(c) The wear resistance of the coatings is found to increase with the increase in alumina reinforcement up to Ni-B-10. However, when the concentration of nanoparticles in the coating bath is increased to 12.5 g/l. the wear resistance decreases as compared to Ni-B-10, due to the increase in the agglomeration of the nanoparticles as well as decrease in elastic modulus.
(d) Ni-B-10 coating displayed the least specific wear rate, i.e., the highest wear resistance amongst all the coatings under study.
(e) Ni-B-10 coating shows a decrease of 77 % in the I_{corr} values and an increase of around 15% in the E_{corr} value as compared to the binary Ni-B coating.

In the present study, Ni-B-10 coating has the most balanced response to the mechanical, tribological and corrosion-resistant properties. With further increase in the concentration of alumina nanoparticles to 12.5 g/l, the wear resistance, elastic modulus and corrosion resistance decrease. Hence, amongst the coatings considered in the present study the Ni-B-10 coating seems to be the most appropriate for use where coatings with low wear rate and high corrosion resistance are required.

REFERENCES

Abdel-Gawad, S. A., Sadik, M. A., &Shoeib, M. A. (2019). Preparation and properties of a novel nano Ni-B-Sn by electroless deposition on 7075-T6 aluminum alloy for aerospace application, Journal of Alloys and Compounds, 785, 1284–1292.

Barati, Q., & Hadavi, S. M. M. (2020). Electroless Ni-B and Composite Coatings: A Critical Review on Formation mechanism, Properties, Applications and Future trends. Surfaces and Interfaces, 100702.

Barman, M., Barman, T. K., & Sahoo, P. (2019). Effect of borohydride concentration on tribological and mechanical behavior of electroless Ni-B coatings. Materials Research Express, 6(12), 126575.

Biswas, A., Das, S. K., & Sahoo, P. (2017). Correlating tribological performance with phase transformation behavior for electroless Ni-(High) P coating, Surface and Coatings Technology, 328, 102–114.

Bülbül, F., Altun, H., Küçük, Ö., &Ezirmik, V. (2012). Tribological and corrosion behaviour of electroless Ni-B coating possessing a blackberry like structure, Metals and Materials International, 18(4), 631–637.

Çelik, I., Karakan, M., &Bülbül, F. (2016). Investigation of structural and tribological properties of electroless Ni-B coated pure titanium, Proceedings of Institution of Mechanical Engineers Part J: Journal of Engineering Tribology, 230(1), 57–63.

Correa, E., Zuleta, A. A., Guerra, L., Gomez, M. A., Castano, J. G., Echeverria, F., Liu, H., Skeldon, P., & Thompson, G. E. (2013). Tribological behavior of electroless Ni–B coatings on magnesium and AZ91D alloy, Wear, 305(1-2), 115–123.

Cullity, B. D., & Stock, S. R. (2001). Elements of x-ray diffraction. NJ: Prentice Hall.

Das, S. K., & Sahoo, P. (2011). Tribological characteristics of electroless Ni-B Coating and optimization of coating parameters using Taguchi based grey relational analysis, Materials & Design, 32(4), 2228–2238.

Delaunois, F., & Lienard, P. (2002). Heat treatments for electroless nickel – boron plating on aluminium alloys, 160, 239–248.

Dervos, C. T., Novakovic, J., &Vassiliou, P. (2004). Vacuum heat treatment of electroless Ni-B coatings, Materials Letters, 58(5), 619–623.

Domínguez-Ríos, C., Hurtado-Macias, A., Torres-Sánchez, R., Ramos, M. A., & González-Hernández, J. (2012). Measurement of mechanical properties of an electroless Ni-B coating using nanoindentation, Industrial & Engineering Chemistry Research, 51(22), 7762–7768.

Ekmekci, D., & Bulbul, F. (2015). Preparation and characterization of electroless Ni–B/Nano-SiO_2, Al_2O_3, TiO_2 and CuO composite coatings, Bulletin of Materials Science, 38(3), 761–768.

Ernst, P., Wadsworth, L. P., & Marshall, G. W. (1997). Porosity of electroless nickel coatings investigated using different porosity tests and their application, Transactions of the Institute of Metal Finishing, 75(5), 194–198.

Freitas, C., & Müller, R. H. (1998). Effect of light and temperature on zeta potential and physical stability in solid lipid nanoparticle (SLN™) dispersions, International Journal of Pharmaceutics, 168(2), 221–229.

Gawne, D. T., & Ma, U. (1987). Wear mechanisms in electroless nickel coatings, Wear, 120(2), 125–149.

Georgiza, E., Gouda, V., & Vassiliou, P. (2017). Production and properties of composite electroless Ni-B-SiC coatings. Surface and Coatings Technology, 325, 46-51.

Hamid, Z. A., Hassan, H. B., &Attyia, A. M. (2010). Influence of deposition temperature and heat treatment on the performance of electroless Ni-B films, Surface and Coatings Technology, 205(7), 2348–2354.

Hu, R., Su, Y., Liu, Y., Liu, H., Chen, Y., Cao, C., & Ni, H (2018). Deposition process and properties of electroless Ni-P-Al_2O_3 composite coatings on magnesium alloy, Nanoscale Research Letters, 13, Article ID: 198.

Hunter, R. J. (2013). Zeta potential in colloid science: Principles and Applications, Academic press.

Islam,M., Azhar,M.R., Khalid, Y., Khan, R., Abdo,H.S., Dar,M.A., Oloyede, O.R., & Burleigh, T.D. (2015). Electroless Ni-P/SiC Nanocomposite Coatings with Small Amounts of SiC Nanoparticles for Superior Corrosion Resistance and Hardness, Journal of Materials Engineering and Performance, 24(12), 4835-4843.

ISO 13099-12012(E) (2012). International Standardization Organization: Colloidal systems-methods for zeta-potential determination-Part 1: Electroacoustic and electrokinetic phenomena.

Jiang, J., Oberdörster, G., & Biswas, P. (2009). Characterization of size, surface charge, and agglomeration state of nanoparticle dispersions for toxicological studies, Journal of Nanoparticle Research, 11(1), 77–89.

Krishnaveni, K., Sankara Narayanan, T. S. N., & Seshadri, S. K. (2012). Electroless Ni-B-Si3N4 composite coating: deposition and evaluation of its characteristic properties, Synthesis and Reactivity in Inorganic, Metal-Organic, and Nano-Metal Chemistry, 42(7), 920–927.

Kumar, A., & Dixit, C. K. (2017). Methods for characterization of nanoparticles, Advances in nanomedicine for the delivery of therapeutic nucleic acids, Elsevier Inc., pp. 44–58.

Laha, T., Balani, K., Agarwal, A., Patil, S., & Seal, S. (2005). Synthesis of nanostructured spherical aluminum oxide powders by plasma engineering, Metallurgical and Materials Transactions A: Physical Metallurgy and Materials Science, 36A (2), 301–309.

León-Patiño, C. A., García-Guerra, J., & Aguilar-Reyes, E. A. (2019). Tribological characterization of heat-treated Ni-P and Ni-P-Al2O3 composite coatings by reciprocating sliding tests, Wear, 426–427, 330–340.

Li, B., Li, X., Huan, Y., Xia, W., & Zhang, W. (2018). Influence of alumina nanoparticles on microstructure and properties of Ni-B composite coating, Journal of Alloys and Compounds, 762, 133–142.

Lu, G. W., & Gao, P. (2010). Emulsions and microemulsions for topical and transdermal drug delivery, Handbook of non-invasive drug delivery systems, Elsevier, pp. 59–94.

Maestro, A., Santini, E., Zabiegaj, D., Llamas, S., Ravera, F., Liggieri, L., Ortega, F., Rubio, R. G., & Guzman, E. (2015). Particle and particle-surfactant mixtures at fluid interfaces: assembly, morphology, and rheological description, Advances in Condensed Matter Physics, 2015, Article ID 917516, 17 pages.

Mahbubul, I. M., Elcioglu, E. B., Amalina, M. A., & Saidur, R. (2019). Stability, thermophysical properties and performance assessment of alumina–water nanofluid with emphasis on ultrasonication and storage period. Powder Technology, 345, 668-675.

Mahdavi, S., Asghari-Alamdari, A., & Zolola-Meibodi, M. (2020). Effect of alumina particle size on characteristics, corrosion, and tribological behavior of Co/Al2O3 composite coatings, Ceramics International, 46(4), 5351–5359.

Mandal, D., Sharma, L. K., & Mukherjee, S. (2016). Defect-induced weak ferromagnetism in transition metal-doped ZnO nanoparticles, Applied Physics A: Materials Science and Processing, 122(12), 1–10.

Manning, P. E. (1980). The effect of scan rate on pitting potentials of high-performance alloys in acidic chloride solution, Corrosion, 36(9), 468–474.

Mohanty, D., Barman, T. K., & Sahoo, P. (2019). Characterisation and corrosion study of electroless Nickel-Boron coating reinforced with alumina nanoparticles, Materials Today: Proceedings, 19(2), 317–321.

Mukhopadhyay, A., Barman, T. K., & Sahoo, P. (2018). Tribological behavior of electroless Ni-B-Mo coatings under dry and lubricated conditions and corrosion resistance in 3.5% NaCl solution. Jurnal Tribologi 18, pp.108-123.

Mukhopadhyay, A., Barman, T. K., & Sahoo, P. (2019). Friction and wear performance of electroless Ni-B coatings at different operating temperatures. Silicon, 11(2), 721-731.

Mukhopadhyay, A., Barman, T. K., Sahoo, P., & Davim, J. P. (2018). Comparative Study of Tribological Behavior of Electroless Ni–B, Ni–B–Mo, and Ni–B–W Coatings at Room and High Temperatures. Lubricants, 6(3), 67.

Narayanan, T. S. N. S., & Seshadri, S. K. (2004). Formation and characterization of borohydride reduced electroless nickel deposits, Journal of Alloys and Compounds, 365, 197–205.

Ordóñez, F., Chejne, F., Pabón, E., & Cacua, K. (2020). Synthesis of ZrO2 nanoparticles and effect of surfactant on dispersion and stability. Ceramics International, 46(8), 11970-11977.

Pal, S., & Jayaram, V. (2018). Effect of microstructure on the hardness and dry sliding behavior of electroless Ni–B coating. Materialia, 4, 47-64.

Pancrecious, J. K., Deepa, J. P., Jayan, V., Bill, U. S., Rajan, T. P. D., & Pai, B. C. (2018). Nanoceria induced grain refinement in electroless Ni-B-CeO2 composite coating for enhanced wear and corrosion resistance of Aluminium alloy. Surface and Coatings Technology, 356, 29-37.

Purohit, P., & Vagge, S. T. (2016). Evaluation of alumina incorporated combined ceramic layer thermal barrier coating, Surface and Coatings Technology, 307, 871–878.

Ruan, H. D., Frost, R. L., & Kloprogge, J. T. (2001). Comparison of Raman spectra in characterizing gibbsite, bayerite, diaspore and boehmite, Journal of Raman Spectroscopy, 32(9), 745–750.

Sahoo, P., & Das, S. K. (2011). Tribology of electroless nickel coatings - A review, Materials & Design, 32(4), 1760–1775.

Sarbishei, S., Faghihi Sani, M. A., & Mohammadi, M. R. (2016). Effects of alumina nanoparticles concentration on microstructure and corrosion behavior of coatings formed on titanium substrate via PEO process, Ceramics International, 42(7), 8789–8797.

Sha, W., Wu, X., & Keong, K. G. (2011). Introduction to electroless copper and nickel–phosphorus (Ni–P) depositions, Electroless Copper and Nickel–Phosphorus Plating, Elsevier, pp. 1–12.

Shakoor, R. A., Kahraman, R., Gao, W., & Wang, Y. (2016). Synthesis, characterization and applications of electroless Ni-B coatings-a review. Int J Electrochem Sci, 11, 2486-2512.

Sudagar, J., Lian, J., & Sha, W. (2013). Electroless nickel, alloy, composite and nano coatings – A critical review, Journal of Alloys and Compounds, 571, 183–204.

Vitry, V., & Bonin, L. (2017). Increase of boron content in electroless nickel-boron coating by modification of plating conditions. Surface and Coatings Technology, 311, 164-171.

Xu, M., Zhang, W., Pei, X., Jiang, J., Cui, Z., & Binks, B. P. (2017). CO_2/N_2 triggered switchable pickering emulsions stabilized by alumina nanoparticles in combination with a conventional anionic surfactant, RSC Advances, 7(47), 29742–29751.

Yildiz, R. A., Genel, K., & Gulmez, T. (2021). Effect of electroless Ni-B and Ni-WB coatings on the corrosion-fatigue behaviour of 7075 Al alloy. International Journal of Fatigue, 144, 106040.

Yu, L., Huang, W., & Zhao, X. (2011). Preparation and characterization of Ni–P–nanoTiN electroless composite coatings, Journal of Alloys and Compounds, 509(10), 4154-4159.

Ziyuan, S., Deqing, W., &Zhimin, D. (2006). Nanocrystalline Ni-B coating surface strengthening pure copper, Applied Surface Science, 253(3), 1051–1054.